High Temperature Deformation Behavior and Constitutive Modeling for Flow Behavior of Alloy 718

Rajesh Jarugula, U. Aravind, Bhagwan Singh Meena, and Subramanian Ganesh Sundara Raman

In the present work, hot deformation behavior of Alloy 718 was investigated over a temperature range of 1223–1373 K and strain rate range of 10^{-2}–10 s^{-1}. The flow curves were corrected for adiabatic temperature rise, particularly at high strain rates. Arrhenius type constitutive equations were derived for Alloy 718 to model the peak flow stress from apparent and physically based approaches. A stress exponent of 5 was obtained from the power-law equation, indicating that the deformation is governed by the dislocation climb mechanism within the aforementioned processing domain. Further, to model the flow behavior, a generalized constitutive equation was derived in which the effect of strain on the flow stress was incorporated. In addition, artificial neural networks (ANN) method was also employed to model the flow behavior. Statistical parameters such as regression coefficient (R) and average absolute relative error (AARE) indicated that the ANN method was more accurate in predicting the flow behavior with $R = 0.99$ and AARE = 0.79% compared to the apparent-based constitutive equation with $R = 0.99$ and AARE = 4.5%. Accuracy of the derived constitutive equation as a material model in finite element (FE) simulation studies was also evaluated. Flow curve predictions obtained from the FE simulation were comparable to the experimental results. The microstructure and hardness at different locations in the deformed samples were consistent with the strain distribution map generated by the FE simulation.

1. Introduction

Alloy 718 is widely used in gas turbines, power generators, rocket engines, metal forming dies and containers. It possesses a combination of good mechanical properties and corrosion resistance up to 923 K. The main strengthening mechanism of this material is the precipitation of ordered-gamma double prime (γ''), which is coherent with the matrix and it acts as a strong barrier for the dislocation movement (Ref 1-3). In addition, the alloy also has other important phases such as delta phase and Laves phase (Ref 4-6). One of the major applications of Alloy 718 is turbine disks, which encounter both high stresses and temperatures (Ref 7). Several researchers investigated the flow behavior and microstructure evolution during deformation of different Ni-based alloys and developed processing maps (Ref 2, 8-14). Alloy 718 is very difficult to be formed due to its high resistance to deformation and shows a very narrow processing window to obtain the completely dynamic recrystallized structure.

Rajesh Jarugula, U. Aravind, and **Subramanian Ganesh Sundara Raman**, Department of Metallurgical and Materials Engineering, Indian Institute of Technology Madras, Chennai 600036, India; and **Bhagwan Singh Meena**, Department of Metallurgical and Materials Engineering, Indian Institute of Technology Madras, Chennai 600036, India; and Armouring Department, Mishra Dhatu Nigam Limited, Hyderabad 500058, India. Contact e-mail: rajeshjarugula@gmail.com.

It is known that the properties of manufactured products depend largely on the microstructure of the material. Understanding the material flow behavior is critical in identifying the processing parameters required to achieve the desired microstructure. Generally, hot deformation of materials involves several metallurgical mechanisms such as work hardening, dynamic recrystallization, dynamic recovery and flow instability. All these cause evolution of a complex microstructure during the processing. However, in order to achieve the required final microstructure and mechanical properties, the hot working parameters (temperature, strain rate and strain) have to be optimized (Ref 15, 16). Over the past decades, numerous efforts have been made to study the optimization of hot working parameters using mathematical and physical simulations.

Advanced numerical techniques such as finite element method, crystal plasticity method and artificial neural networks (ANN) are employed to optimize the thermo-mechanical processing parameters (Ref 17-23). Simulation studies also help to predict the evolution of microstructure of materials during hot working processes. In finite element simulations, the material flow behavior is modeled by a constitutive equation. A constitutive equation is a mathematical relation which is derived from experimental data relating the flow stress of materials and the hot working process parameters. The accuracy and reproducibility of finite element simulations depend largely on the constitutive equation used. Thus, it is important that a derived constitutive equation should be validated for its accuracy to be used as a generalized material model in finite element studies (Ref 24-27).

To control the evolution of microstructure during hot deformation, it is important to know the stress at which dynamic recrystallization initiates. Knowing this value of critical stress also helps in the modeling of hot working processes accurately. However, it is difficult to obtain the

critical stress value directly from the flow curves. To calculate the flow curve characteristics (critical stress, peak stress, peak strain, steady state stress and saturated stress) a method has been proposed by Poliak and Jonas (Ref 28). According to that method, the occurrence of the inflection point in the plot between strain hardening rate $\left(\theta = \left(\frac{d\sigma}{d\varepsilon} \right)_{T,\dot{\varepsilon}} \right)$ and flow stress corresponds to the critical stress value, and the peak stress is obtained from the same plot at $\theta = 0$. Here σ is flow stress (MPa), ε is strain, T is temperature (K) and $\dot{\varepsilon}$ is strain rate (s^{-1}).

The reported values of critical stress values normalized with respect to peak stress for 17-4 PH stainless steel, 304H austenitic stainless steel and medium carbon steel are 0.89, 0.875 and 0.879, respectively (Ref 29-31). Therefore, it is reasonable to consider that the peak stress is almost equal to the critical stress required to the onset of dynamic recrystallization (DRX) and it can be assumed that DRX begins at peak stress value.

Thomas et al. (Ref 2) investigated the hot deformation behavior of Alloy 718 over a range of temperatures (1173–1353 K) and strain rates (5×10^{-4}-10^{-1} s^{-1}). Before hot compression testing, the samples were annealed at 1353 K for 1 h in order to homogenize the microstructure. They reported that the homogenization temperature did not dissolve all precipitates and some second phase particles remained undissolved. These second phase particles promoted some hardening during deformation at 1173 K and influenced the deformation mechanism. Wang et al. (Ref 32) studied the hot deformation behavior of delta-processed Alloy 718 over a range of temperature (1223-1373 K) and strain rates (10^{-3}-1 s^{-1}) mainly to understand the evolution of δ phase during hot deformation as well as the mechanisms of DRX. The main nucleation mechanisms of DRX for the delta-processed Alloy 718 reported by them are bulging of original grain boundaries and the δ phase stimulated DRX nucleation, which is dependent on the dissolution behavior of the δ phase. Tan et al. (Ref 11) conducted studies on the hot deformation behavior of fine grained Alloy 718 and proposed a constitutive equation. Recently, Pedro et al. (Ref 33) carried out the hot compression tests at two temperatures of 1233 K and 1293 K (below and above the δ-solvus temperature) on delta-processed Alloy 718. They reported partial dissolution and fracture of δ phase during the deformation resulting in fine and distributed δ particles near grain boundaries which were presumed to act as nucleation sites for DRX. Further, in that study they employed Estrin–Mecking–Bergstrom approach (Ref 34, 35) to model the flow behavior up to peak stress. Gujrati et al. (Ref 36) studied the relation between activation energy of hot deformation and deformation mechanisms in Alloy 718. Also, flow stress modeling was carried out using Schöcks–Seeger–Wolf, Kocks and Sellers models. Gupta et al. (Ref 37) correlated deformation parameters with microstructural evolution during hot deformation in Alloy 718. The processing parameters were optimized using processing map approach. Kumar et al. (Ref 38) studied the hot deformation of hot isostatically processed nickel-base superalloy and reported significant change in the flow stress due to adiabatic temperature rise, particularly at lower temperatures and high strain rates. However, most of the above reported studies have not considered the change in flow stress due to adiabatic temperature rise, nor the effect of strain on the flow stress. But in Ni-based alloys, it is observed that the flow stress varies with the strain. Hence, while modeling the flow curve, it is necessary to compensate the effect of strain in the constitutive equation.

In most of the above-mentioned research efforts, a constitutive equation was derived for Alloy 718, but there was no validation of the constitutive equation. Generally, a constitutive equation analysis involves linear regression of the experimental data. The derived constitutive equation might be confined to a limited processing domain where specific deformation mechanisms operate in the material. Therefore, the derived constitutive equation may not be accurate enough to predict the flow behavior when the flow stress exhibits nonlinear dependence on the processing parameters and also in experimental conditions which are different from the experimental conditions for which constitutive equation has been derived. In these conditions, ANN technique offers a more flexibility to describe the flow behavior over constitutive equation approach. Basically, ANN learns, memorizes and recognizes the data pattern during the training procedure without any prior assumption about their nature (Ref 39). Though ANN does not incorporate the physical knowledge about deformation behavior and restoration mechanisms, it is able to describe the flow behavior very accurately (Ref 39-41). In addition, studies on understanding the deformation mechanisms operating at the hot working temperatures are also scarce. It has been reported that the physically based approach can provide an insight of governing deformation mechanisms (Ref 42). Based on these inferences, the objective of present work is defined.

The main objective of the present work is to investigate the flow behavior and deformation mechanisms of Alloy 718 in a solution treated condition over a range of temperatures (1223–1373 K) and strain rates (10^{-2}–10 s^{-1}) and to derive a constitutive equation by employing the apparent and physically based approaches. Also, an effort has been made to develop a generalized constitutive equation that considers the effect of strain on the flow stress and to validate the accuracy of the developed equation as a generalized material model by finite element simulation studies. In addition, the ANN method was also employed to study the flow behavior. Further, statistical parameters (regression coefficient and average absolute relative error) were employed to evaluate the performance of models. Finite element simulation was used to understand the strain distribution in samples after the deformation.

2. Experimental Procedure

The material used in this work is Alloy 718 and its nominal composition is listed in Table 1. The initial material, supplied in the extruded rod form, was solution treated for 4 h at 1373 K. The solution treatment temperature was selected based on the study by Wang et al. (Ref 32) in which the same temperature of 1373 K was used for solution treatment for superalloy 718. However, the treatment time used by them was 30 min. In an another study to investigate the effect of grain size of alloy 718 (unpublished work), the authors of the present paper varied the treatment duration from 10 min to 4 h at 1373 K. In the present work, 4 h solution treatment duration was chosen. After the heat treatment, cylindrical samples of dimensions 10 mm in diameter and 15 mm in length were cut using a wire cut electric discharge machine. Isothermal uniaxial compression tests were carried out in the Gleeble 3800 thermo-mechanical simulator at different temperatures of 1223, 1273, 1323 and 1373 K and

Table 1 Chemical composition (in wt.%) of test material Alloy 718

Ni	Cr	Fe	Nb	Mo	Ti	Al	V	Mn	S	C	B
51.6	18.2	19.76	5.1	3.28	1.06	0.56	0.33	0.09	0.01	0.004	0.003
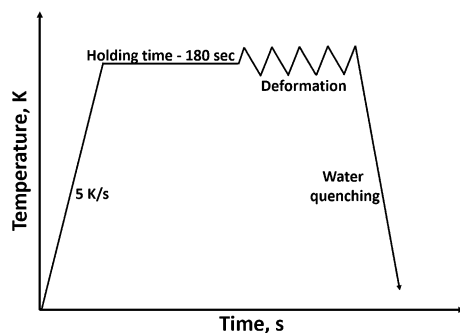
Fig. 1 Schematic of experimental procedure

different strain rates of 10^{-2}, 10^{-1}, 1 and 10 s^{-1}. During deformation, to reduce the friction between anvils and sample, a graphite sheet along with nickel paste was used as lubricant. The schematic shown in Fig. 1 explains the experimental procedure. Initially, the samples were heated to the testing temperature at a rate of 5 K/s and held at the testing temperature for 180 s and then compressed. Afterward, the deformed samples were water quenched in the testing chamber using two jets immediately after finishing the test. The total true strain given to the samples during deformation is 0.7. The true stress–true strain data were recorded using a data acquisition system.

3. Results and Discussion

3.1 Initial Microstructure

The microstructure of Alloy 718, solution treated for 4 h at 1373 K, shows equi-axed grain structure with an average grain size of 120 μm.

3.2 Flow Curve Behavior

The true stress–true strain curves measured at different temperatures and strain rates are shown in Fig. 2. It is observed that for all test conditions flow stress is decreasing with increasing temperature and decreasing strain rate. In the initial stage of the flow curve, the flow stress is increasing with increasing strain due to strain hardening (increase in dislocation density), and once it reaches peak stress, flow softening (dynamic recovery) is observed. However, at lower strain rates (10^{-2} and 10^{-1} s^{-1}) steady state flow is observed after the peak stress with increasing strain, which occur when a balance between strain hardening and dynamic softening is attained. A similar type of flow behavior has been reported in Alloy 718 and other Ni-based alloys possessing low stacking fault energy, which indicates the DRX phenomenon during the deformation (Ref 9, 43, 44).

It is worth to mention that, particularly at higher strain rates (1 and 10 s^{-1}) more flow softening is observed compared to that at the lower strain rates (10^{-2} and 10^{-1} s^{-1}) and this is attributed to adiabatic temperature rise (ATR) at higher strain rates. A thermocouple was welded on the periphery of the sample and the temperature rise in the sample was recorded online during the experiment. The variation in temperature rise for all strain rates at a temperature of 1223 K is shown in Fig. 3(a). The ATR (ΔT) at strain rates of 1 and 10 s^{-1} at each temperature is shown in Fig. 3(b). Subsequently, change in the stress ($\Delta\sigma$) due to ATR is estimated by using an expression (Eq 1). The extent of ATR is decreasing with increasing the temperature and corrected flow stress due to ATR is also included in Fig. 2. As Ni exhibits poor thermal conductivity ($\sim$ 14.7 W/m K), the heat generated due to plastic deformation at higher strain rates has very less time to get dissipated from the sample and this causes the localized heating. The combination of large stored energy and adiabatic temperature rise enhances the dynamic recrystallization fraction at higher strain rates (Ref 11, 15, 45). The optical micrographs of samples deformed at 1373 K for different strain rates are presented in Fig. 4. It clearly seen that fraction of dynamic recrystallized grains increases with an increase in strain rate;

$$\Delta\sigma = \Delta T \left(\frac{d\sigma}{dT}\right)_{\varepsilon,\dot{\varepsilon}} \tag{Eq 1}$$

3.3 Constitutive Equation Analysis

3.3.1 Apparent-Based Approach. In hot deformation, the flow stress highly depends on temperature and strain rate is described by an Arrhenius equation The effects of temperature and strain rate on deformation behavior are incorporated in the Zener–Hollomon parameter (Z), which is temperature compensated strain rate (Ref 46). In most of the previous studies, flow stress is modeled by an expression that relates the Zener–Hollomon parameter (Z) and flow stress (σ) as (Ref 47):

$$Z = \dot{\varepsilon}\exp\left(\frac{Q}{RT}\right) = f(\sigma) \tag{Eq 2}$$

where $\dot{\varepsilon}$ is strain rate (s^{-1}), Q is the activation energy (J/mol), R is the gas constant (J/mol K), T is the temperature (K).

Since both creep and hot working are considered as thermally activated processes, for hot deformation analysis, strain rate equations similar to those used in the creep studies are used. Generally, Arrhenius type equations are used to describe the relation among the flow stress, temperature and strain rate as:

$$\dot{\varepsilon} = Af(\sigma)\exp\left(\frac{-Q}{RT}\right) \tag{Eq 3}$$

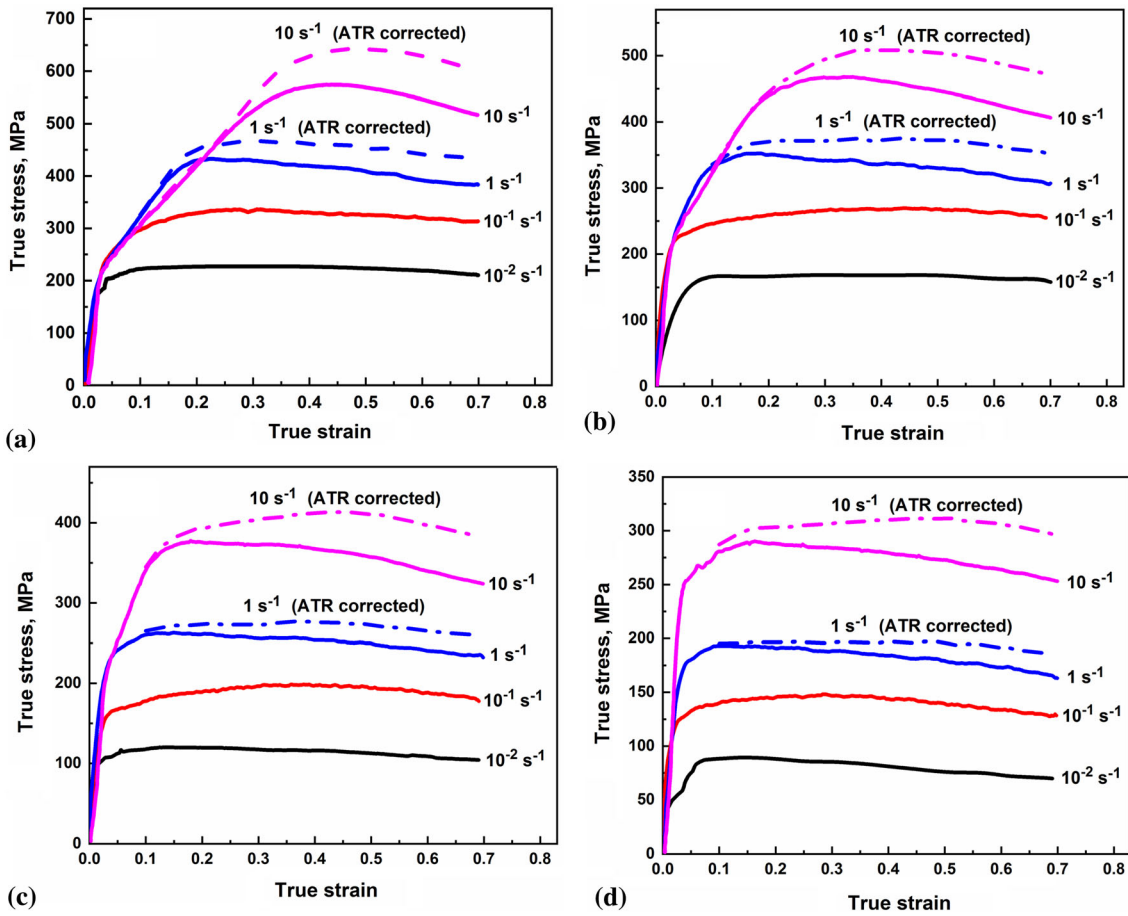$$\dot{\varepsilon} = A_1\sigma^n\exp\left(\frac{-Q}{RT}\right) \tag{Eq 4}$$

Fig. 2 True stress–true strain curves for Alloy 718 at different temperatures: (a) 1223 K, (b) 1273 K, (c) 1323 K and (d) 1373 K
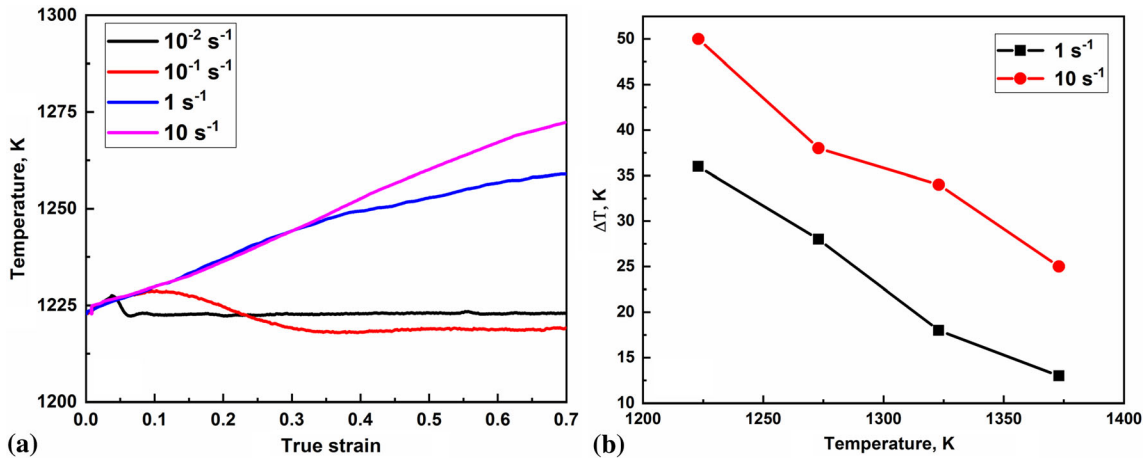

Fig. 3 (a) Variation of temperature with the strain during the tests conducted at 1223 K and different strain rates, (b) Adiabatic temperature rise (ΔT) for tests conducted at different temperatures and two different strain rates

$$\dot{\varepsilon} = A_2 \exp(\beta\sigma) \exp\left(\frac{-Q}{RT}\right) \tag{Eq 5}$$

$$\dot{\varepsilon} = A_3 [\sinh(\alpha\sigma)]^{n_1} \exp\left(\frac{-Q}{RT}\right) \tag{Eq 6}$$

where $\dot{\varepsilon}$ is strain rate (s^{-1}), A, A_1, A_2, A_3, β, n and n_1 are the material constants, Q is the activation energy (J/mol), T is the temperature (K), σ is the flow stress (MPa), R is the gas constant (8.314 J/mol K) and α ($\approx \beta/n$ MPa^{-1}) is the stress multiplier.

The power law (Eq 4) is preferred for lower stresses ($\alpha\sigma < 0.8$), whereas for higher stresses, exponential law (Eq 5) ($\alpha\sigma > 1.2$) is preferred. In addition to that, Sellers–
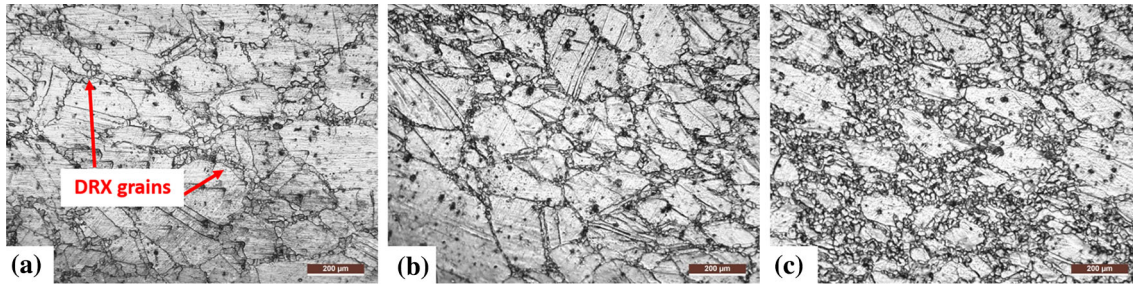
Fig. 4 Optical micrographs of samples deformed at 1373 K and at different strain rates: (a) 10^{-1} s^{-1}, (b) 1 s^{-1} and 10 s^{-1}. Scale bar = 200 μm

Tegart (Ref 48, 49) hyperbolic sine law (Eq 6) suggested by Garofolo (Ref 50) (for all $\alpha\sigma$) is used to cover a wide range of stresses.

From conventional Eq 4 and 6, the obtained values of n, n_1 and Q are referred to as apparent values, because internal microstructure state has not been taken into account. They are derived from the Arrhenius equation with linear regression analysis by assuming that the microstructure remains constant during deformation. Hence, this method is referred to as apparent-based approach. Consequently, from this approach, it is difficult to infer about deformation mechanisms operating in the material (Ref 42).

By applying the natural logarithm on both sides of Eq 4 and 5, the following expressions are obtained to evaluate the peak stress (σ_p).

$$\ln\dot{\varepsilon} + \frac{Q}{R}\left(\frac{1}{T}\right) = \ln A_1 + n\ln\sigma_p \qquad \text{(Eq 7)}$$

$$\ln\dot{\varepsilon} + \frac{Q}{R}\left(\frac{1}{T}\right) = \ln A_2 + \beta\sigma_p \qquad \text{(Eq 8)}$$

Assuming that the activation energy is constant at given temperature, the partial differentiation of Eq 7 and 8 with respect to σ_p, yields the following expressions:

$$n = \left[\frac{\partial\ln\dot{\varepsilon}}{\partial\ln\sigma_p}\right]_T \qquad \text{(Eq 9)}$$

$$\beta = \left[\frac{\partial\ln\dot{\varepsilon}}{\partial\sigma_p}\right]_T \qquad \text{(Eq 10)}$$

The values of n and β were obtained from the slope of the plot between $\ln\dot{\varepsilon}$ and $\ln\sigma_p$ and slope of the plot between $\ln\dot{\varepsilon}$ and σ_p, respectively. The corresponding plots are shown in Fig. 5(a) and (b). The linear regression analysis of the data points at each deformation temperature was performed. The value of slope varies with temperature. Therefore, the average values of n (= 6.06) and β (= 0.02281) were obtained from the average of all slopes, respectively. Eventually, the value of α (= 0.00376 MPa^{-1}) was obtained from the ratio of β/n.

A similar value of α (= 0.0042 MPa^{-1}) was found by Gujrati et al. (Ref 36).

By applying the natural logarithm on both sides of Eq 6, we get the following expression:

$$\ln\dot{\varepsilon} + \frac{Q}{R}\left(\frac{1}{T}\right) = \ln A_3 + n_1\ln\left[\sinh\left(\alpha\sigma_p\right)\right] \qquad \text{(Eq 11)}$$

At constant deformation temperature, the partial differentiation of Eq 11 with respect to σ_p, yields the following expression. The same is used to evaluate the value of n_1.

$$n_1 = \left[\frac{\partial\ln\dot{\varepsilon}}{\partial\ln\left[\sinh\left(\alpha\sigma_p\right)\right]}\right]_T \qquad \text{(Eq 12)}$$

The value of n_1 was obtained from the plot between $\ln\dot{\varepsilon}$ and $\ln\left[\sinh\left(\alpha\sigma_p\right)\right]$ and the corresponding plot is shown in Fig. 6(a). The linear regression analysis of data points was performed at all deformation temperatures. The average value of n_1 (= 4.4) was obtained from the average of all slopes. A similar value of n_1 (= 4.57) was found by Gujrati et al. (Ref 36).

In order to calculate the deformation activation energy, partial differentiation of Eq 11 with respect to (1/T) at constant strain rate, yields the following expression

$$Q = Rn_1\left[\frac{\partial\ln\left[\sinh\left(\alpha\sigma_p\right)\right]}{\partial(1/T)}\right]_{\dot{\varepsilon}} \qquad \text{(Eq 13)}$$

The slopes obtained from the plot $\ln\left[\sinh\left(\alpha\sigma_p\right)\right]$ against (1000/T) were used to calculate the Q value. The corresponding plot is shown in Fig. 6(b). The linear regression analysis of the data points was performed at all strain rates. The average value from all the slopes was considered to estimate the Q value. The Q value obtained from hyperbolic sine law is 478 kJ/mol. Earlier, similar Q values were reported by researchers in the literature for Alloy 718 subjected to hot deformation, e.g., Yuan and Liu (443 kJ/mol) (Ref 51), Weis (423 kJ/mol) (Ref 52), Garcia et al. (485 kJ/mol) (Ref 53), Tan et al. (406.5 kJ/mol) (Ref 11). However, in all these studies including the present study, the estimated Q value is quite higher than the self-diffusion activation energy (Q_{sd}) of nickel (285 kJ/mol) (Ref 54). The difference in the estimated Q and Q_{sd} of nickel is attributed to the complex alloy chemistry and microstructural characteristics (Ref 38, 55). Bi et al. (Ref 56) investigated the effect of concentration of alloying elements on the evolution of Q in nickel-based superalloys. It was found that the presence of different alloying elements like Cr, Ti, Mo, Nb and W invariably increases the Q value with increasing weight fraction. In addition to these factors, Tan et al. (Ref 11) reported that the Q value in Alloy 718 is dependent on the initial grain size and a decrease in grain size results in lower Q. Recently, Gujrati et al. (Ref 36) reported the Q value of 364 kJ/mol for Alloy 718 and the discrepancy in Q compared to Q_{sd} is attributed to occurrence of DRX during hot deformation.

Finally, the relation between the peak stress and Zener parameter was obtained by plotting ln [sinh ($\alpha\sigma_p$)] against lnZ
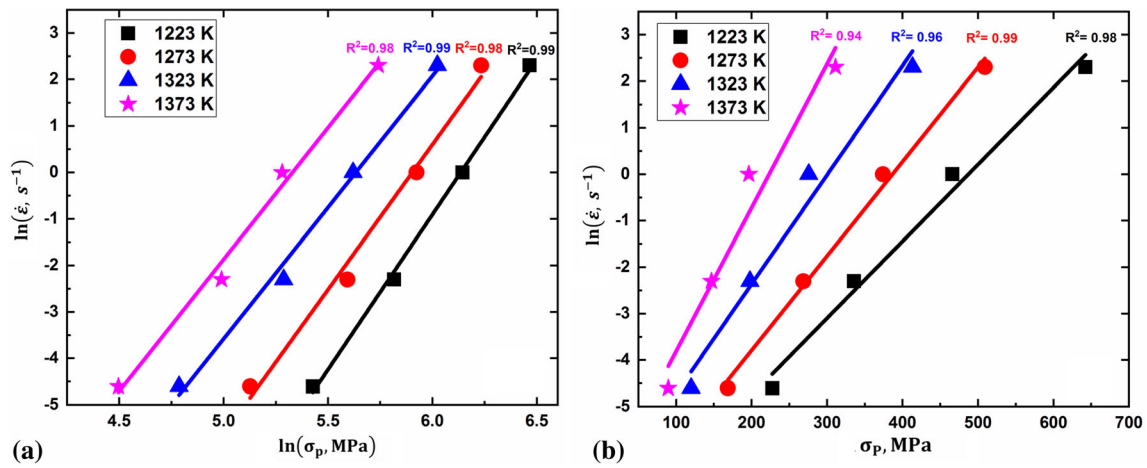
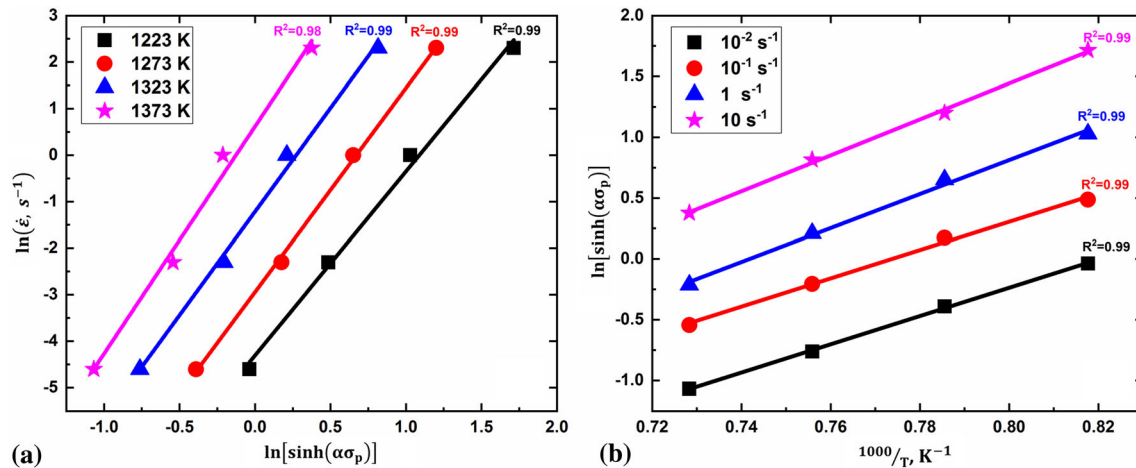**Fig. 5** (a) Plot of $\ln \dot{\varepsilon}$ versus $\ln \sigma_p$, (b) plot of $\ln \dot{\varepsilon}$ versus σ_p

Fig. 6 (a) Plot of $\ln \dot{\varepsilon}$ versus $\ln\left[\sinh\left(\alpha\sigma_p\right)\right]$, (b) plot of $\ln\left[\sinh\left(\alpha\sigma_p\right)\right]$ versus $\frac{1000}{T}$

for hyperbolic sine law and the corresponding plot is shown in Fig. 7. The slope and intercept obtained from the plots are the final values of n_1 and A_3, respectively. The linear regression analysis of the data resulted in the following equation:

$$Z = \dot{\varepsilon}\exp\left(\frac{477389}{RT}\right) = 3.07 \times 10^{18} \times \left[\sinh\left(0.00376x\sigma_p\right)\right]^{4.4}$$

(Eq 14)

The values of experimental peak stresses are plotted against the predicted peak stresses calculated from the constitutive Eq 15 corresponding to hyperbolic sine law in Fig. 8. The predicted peak stress values are in good agreement with the experimental peak stress values.

$$\sigma_p = \frac{1}{\alpha}\sinh^{-1}\left(\frac{Z}{A_3}\right)^{1/n_1} = \frac{1}{0.00376}\sinh^{-1}\left(\frac{\dot{\varepsilon}\exp\left(\frac{477389}{RT}\right)}{3.07 \times 10^{18}}\right)^{1/4.4}$$

(Eq 15)

3.3.2 Physically Based Approach. The activation energy for hot deformation obtained from the apparent-based approach is 478 kJ/mol, which is quite distinct and higher than the
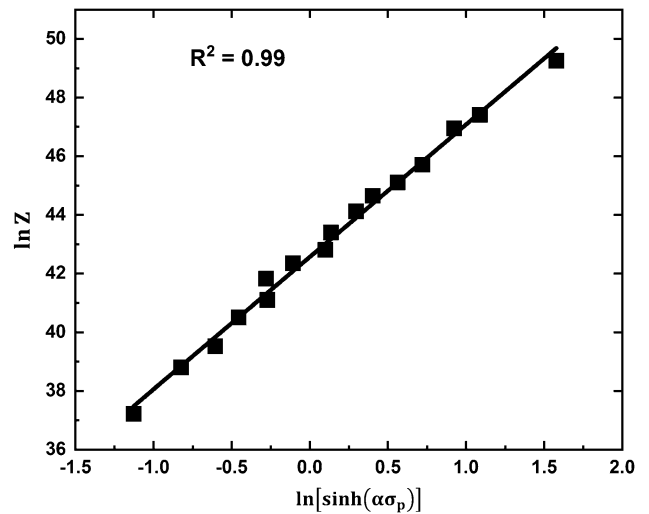

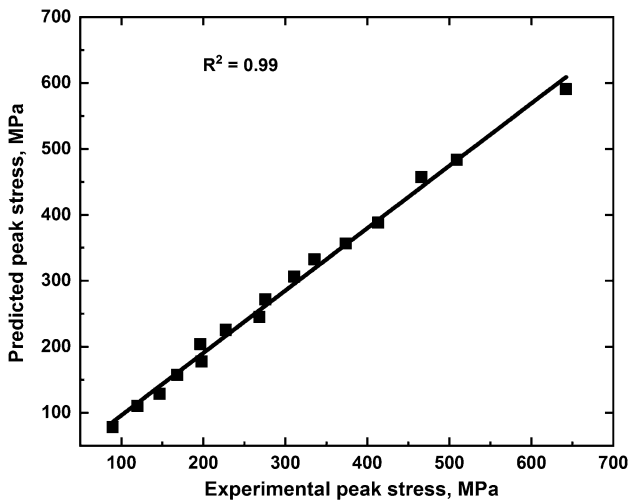**Fig. 7** Plot of $\ln Z$ versus $\ln\left[\sinh\left(\alpha\sigma_p\right)\right]$

Fig. 8 Comparison of predicted peak stress and experimental peak stress

activation energy for self-diffusion of pure Ni. Hence, it is difficult to infer about deformation mechanism from the apparent-based approach. Thomas et al. (Ref 2) have shown that if the deformation mechanism is controlled by dislocation climb, a constant stress exponent and activation energy for self-diffusion of a studied material can be used in the Sellers equation to describe the appropriate stress by incorporating the influence of temperature dependence of Young's modulus and self-diffusion coefficient of the material. Hence, this method is referred to as physically based approach (Ref 42). Accordingly, the modified Sellers equation has been employed to describe the appropriate stress for materials like steels, aluminum alloy (Ref 57-59). The unified equation is expressed as follows:

$$\frac{\dot{\varepsilon}}{D_{(T)}} = B_3 \left[\sinh\left(\alpha' \frac{\sigma}{E_{(T)}} \right) \right]^{n''} \qquad \text{(Eq 16)}$$

where $D_{(T)}$ is self-diffusion coefficient at a temperature, B_3 is material constant, n'' is stress exponent, α' is stress multiplier, $E_{(T)}$ is Young's modulus at a temperature.

Therefore, physically based approach was employed to deduce the deformation mechanisms here and discussed in this section. In this approach, only two unknown parameters (α' and B_3) have to be derived from Eq 16. To determine α', similar approach discussed in Sect. 3.3.1 was employed. The power law and exponential law after including the $D_{(T)}$ and $E_{(T)}$ are expressed as

$$\frac{\dot{\varepsilon}}{D_{(T)}} = B_1 \left[\frac{\sigma_p}{E_{(T)}} \right]^{n'} \qquad \text{(Eq 17)}$$

$$\frac{\dot{\varepsilon}}{D_{(T)}} = B_2 \exp\left(\beta' \frac{\sigma_p}{E_{(T)}} \right) \qquad \text{(Eq 18)}$$

where B_1, B_2 and β' are material constants, n' is true stress exponent.

The temperature dependent shear modulus ($G_{(T)}$) and self-diffusion coefficient ($D_{(T)}$) were calculated using Eq 19 and 20. The values of $D_o = 1.6 \times 10^{-4}$ m^2/s, $Q_{sd} = 285$ kJ/mol and G_o (at 300 K) $= 8.31 \times 10^4$ MPa, corresponding to pure Ni were taken from Ashby tables (Ref 54). The Young's modulus (E)

was obtained by inserting the G values in the following relation (Ref 60) ($E = 2G(1 + v)$) ($v = 0.3$).

$$D_{(T)} = D_o \exp\left(\frac{-Q_{sd}}{RT} \right) \qquad \text{(Eq 19)}$$

$$G_{(T)} = G_o \left(1 - 0.5 \frac{(T - 300)}{T_M} \right) \qquad \text{(Eq 20)}$$

Here n' and β' were obtained from the slope of the plot between $\ln\left(\dot{\varepsilon}/D_{(T)} \right)$ versus $\ln\left(\sigma_P/E_{(T)} \right)$ and $\ln\left(\dot{\varepsilon}/D_{(T)} \right)$ versus $\left(\sigma_P/E_{(T)} \right)$, respectively, see Fig. 9(a) and (b). The $\alpha'(= 549)$ was calculated from the ratio of $\left(\beta'/n' \right)$. The main advantage of this method is that all the data points lie on a single line, which means only a single regression is necessary to obtain α'. On the other hand, in the apparent-based approach, regression analysis has to be performed at each temperature.

A linear fit of the plot between $\left(\dot{\varepsilon}/D_{(T)} \right)^{1/5}$ and $\sinh\left(\alpha'\sigma_P/E_{(T)} \right)$ with an intercept of zero ($y = mx + 0$) was done as shown in Fig. 10(a). The slope of the linear fit gives the value of $(B_3)^{(1/5)} = 673$ from Eq 6. The final resultant physically based constitutive equation can be expressed as:

$$Z = \dot{\varepsilon} \exp\left(\frac{285000}{RT} \right) = 2.2 \times 10^{10} \times \left[\sinh\left(549x\sigma_P/E_{(T)} \right) \right]^5 \qquad \text{(Eq 21)}$$

The comparison between the values of the predicted peak stress calculated from the final Eq 21 corresponding to the physically based approach and the experimental peak stress values is shown in Fig. 10(b).

The interesting observations from the physically based approach are the true stress exponent (n') obtained from the power law, i.e., the slope of the plot between $\ln\left(\dot{\varepsilon}/D_{(T)} \right)$ versus $\ln\left(\sigma_P/E_{(T)} \right)$ is ~ 5. In the present work, from the slope obtained from the plot shown in Fig. 9(a) it is deduced that the dislocation climb is the dominating deformation mechanism operating in the studied temperature and strain rate domain (Ref 54). However, power law is not capable to explain the flow behavior when $\alpha\sigma > 1.2$. Hence, it is always suggested to employ sine hyperbolic law to represent the flow behavior in hot deformation studies since it covers a wide range of stresses.

Earlier, Thomas et al. (Ref 2) studied the effect of aging on the hot deformation of Alloy 718 by using the physically based approach and observed that experimental points obtained at different temperatures did not lie on a single line in the plot between $\ln\left(\dot{\varepsilon}/D_{(T)} \right)$ versus $\ln\left(\sigma_P/E_{(T)} \right)$ like in the present work (particularly tests done at 1173 K and 1223 K). This was attributed to the high stress exponent observed due to the precipitates formed during the aging treatment in the material, further these precipitates hindered the dislocation movement and introduced a back stress.

Both Eq 15 and 21 derived based on the apparent and physically based approaches look almost similar to each other, but the nature of the material constant values are completely different after compensating the temperature effect by means of $D_{(T)}$ and $E_{(T)}$ in Eq 16.
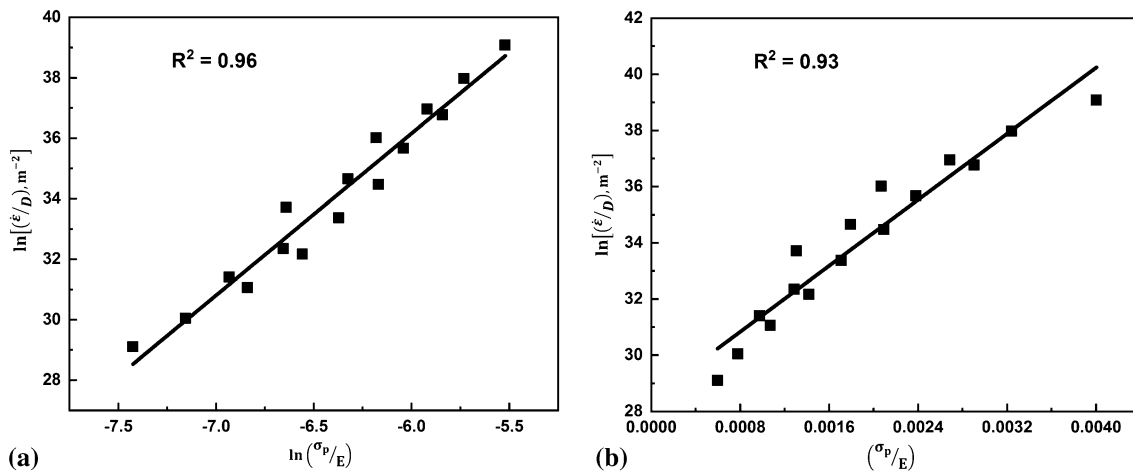
Fig. 9 (a) Plot of $\ln\left(\dot{\varepsilon}/D\right)$ versus $\ln\left(\sigma_P/E\right)$, (b) plot of $\ln\left(\dot{\varepsilon}/D\right)$ versus $\left(\sigma_P/E\right)$
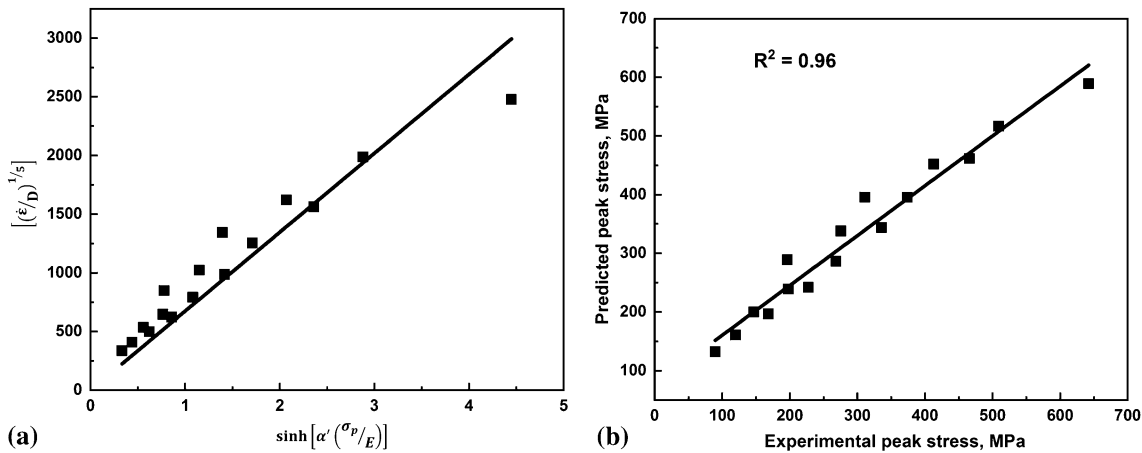

Fig. 10 (a) Plot used to determine B_3, (b) comparison between experimental peak stress and predicted peak stress

3.4 Performance Evaluation of a Constitutive Equation

The prediction capability of a constitutive model is quantified by employing the statistical parameters such as correlating coefficient (R) and average absolute relative error (AARE) which are expressed as follows:

$$R = \frac{\sum_{i=1}^{n}(e_i - \bar{e})(P_i - \bar{P})}{\sqrt{\sum_{i=1}^{n}(e_i - \bar{e})^2 \sum_{i=1}^{n}(P_i - \bar{P})^2}} \quad \text{(Eq 22)}$$

$$\text{AARE}(\%) = \frac{1}{n}\sum_{i=1}^{n}\left|\frac{e_i - p_i}{e_i}\right| \times 100 \quad \text{(Eq 23)}$$

where e_i and e are experimentally measured value and mean value of all the experimental results, P_i and P are predicted value and mean value of all the predicted results calculated from the model, n is the total number of data points considered for the analysis. The correlation coefficient is frequently used to analyze the strength of the linear relationship between experimental and predicted values. When R is close to zero, it indicates that the regression line does not fit the data well and when R is close to 1, it indicates that the regression line fits the data well. However, higher R value always need not indicate the better performance of the model/equation because tendency of model/equation biased toward higher or lower values (Ref 61), whereas AARE is a measure of prediction accuracy of the model and it provides unbiased statistics by computing through term by term comparison of the relative errors (Ref 62).

The peak stress predicted from Eq 21 corresponding to physically based approach have shown a (R) = 0.96 and AARE (18%). On the other hand, in the apparent-based approach, a higher value of R = 0.99 and lower value of AARE = 6% were obtained. This indicates that the apparent-based approach is more reliable than the physically based approach for predicting the peak stress.

3.5 Effect of Strain on the Flow Stress

As mentioned earlier, the effect of strain on the flow stress is not considered in Eq 5 presuming that it has a negligible effect on the flow stress at the hot working temperatures. However, the effect of strain on the flow stress is significant at lower working temperatures. In order to model the entire flow curve, it is inappropriate to use the same material constants obtained at peak stress. This problem could be addressed by incorporating the influence of strain in the constitutive equation. This approach has been firstly described by Rao and Hawbolt (Ref 63) and then critically revised by Mirzadeh (Ref 64). It could be possible by establishing the relation between deformation strain

and material constants (α, n_1, Q and A_3). The material parameters were derived using the above procedure (similar way to derived for peak stress) for a range of strains from 0.1 to 0.7 with an interval of 0.05. After deriving the material parameters for different strains, polynomial equations were used in order to attain a relationship between the deformation strain and material constants as shown in Fig. 11. A fourth-order polynomial Eq 24-27 reasonably fits the entire strain regime and the information about coefficients of polynomial equations is provided in Table 2. Therefore, the material constants can be calculated at any strain in the flow curve from polynomial equations. Subsequently, the flow stress can be predicted from a constitutive Eq 15 at any strain in the flow curve.

$$\alpha = \alpha_0 + \alpha_1\varepsilon + \alpha_2\varepsilon^2 + \alpha_3\varepsilon^3 + \alpha_4\varepsilon^4 \qquad \text{(Eq 24)}$$

$$n_1 = n_0 + n_1\varepsilon + n_2\varepsilon^2 + n_3\varepsilon^3 + n_4\varepsilon^4 \qquad \text{(Eq 25)}$$

$$Q = Q_0 + Q_1\varepsilon + Q_2\varepsilon^2 + Q_3\varepsilon^3 + Q_4\varepsilon^4 \qquad \text{(Eq 26)}$$

$$\ln A_3 = A_0 + A_1\varepsilon + A_2\varepsilon^2 + A_3\varepsilon^3 + A_4\varepsilon^4 \qquad \text{(Eq 27)}$$

The predicted flow stress values obtained from the apparent-based approach is compared with the experimental flow stress at different temperatures and strain rates as shown in Fig. 12. The predicted flow stress results are comparable with the experimental results except the flow stress predicted at temperatures (1223 and 1273 K) and strain rates (1 and 10 s^{-1}). Initially, these curves had shown two stage strain hardening behavior [see Fig. 12(a) and (b)] and it can be noticed from the flow curves that, until strain of 0.25, flow stress at the strain rate of 10 s^{-1} is lower than the flow stress measured at the strain rate of 1 s^{-1}. Therefore, during the evaluation of material constants, the flow stress measured at the strain rate of 10 s^{-1} was not considered in the analysis till strain of 0.25. This might be a plausible reason for the deviation of predicted flow stress from experimental flow curves. The comparison of experimental stress and predicted stress is shown in Fig. 13. Most of the data points are close to the 45° line except a few data points corresponding to (1223 and 1273 K) and strain rates (1 and 10 s^{-1}). The values of R and AARE are 0.98 and 4.5%, respectively.

Table 2 Coefficients for the polynomial equations

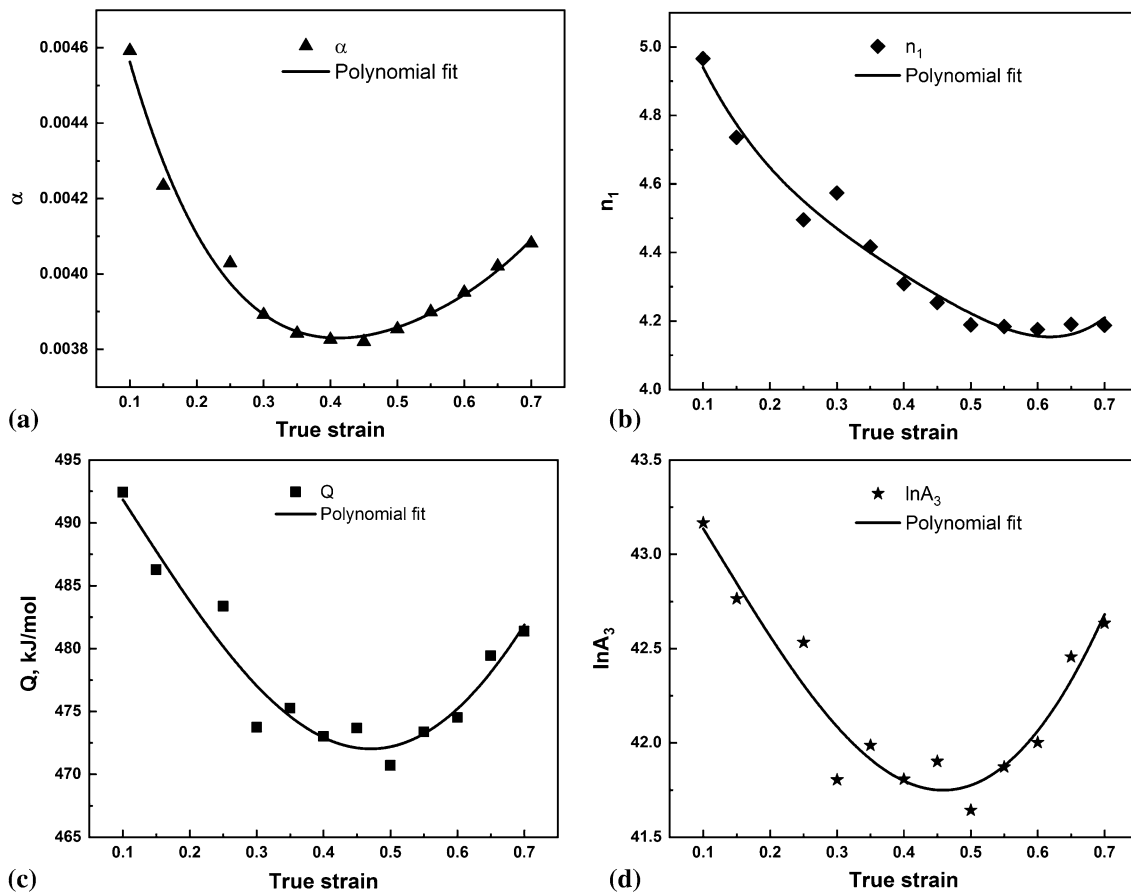| n_1	Q	α	$\ln A_3$
$n_0 = 5.46$	$Q_0 = 499.55$	$\alpha_0 = 0.00538$	$A_0 = 43.67$
$n_1 = -6.9$	$Q_1 = -68.39$	$\alpha_1 = -0.01052$	$A_1 = -4.71$
$n_2 = 19.64$	$Q_2 = -123.81$	$\alpha_2 = 0.02572$	$A_2 = -9.21$
$n_3 = -31.53$	$Q_3 = 395.66$	$\alpha_3 = -0.0279$	$A_3 = 27.59$
$n_4 = 19.87$	$Q_4 = -186.71$	$\alpha_4 = 0.01264$	$A_4 = -11.02$

Fig. 11 Variation of material constants with true strain: (a) α, (b) n_1, (c) Q and (d) $\ln A_3$
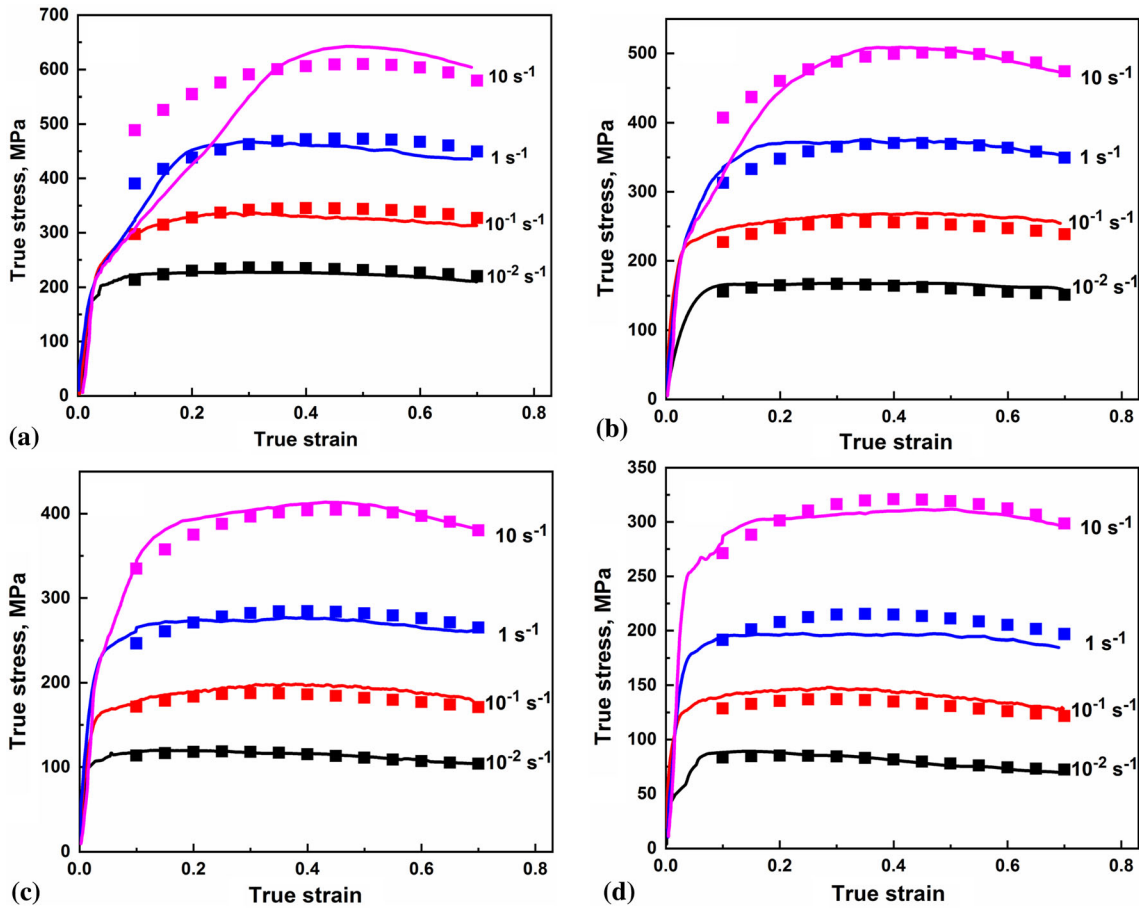
Fig. 12 Comparison between predicted flow stress obtained from a constitutive equation and the experimental flow stress at different strain rates: (a) 1223 K, (b) 1273 K, (c) 1323 K and (d) 1373 K (line represents experimental curve and square symbol represents predicted value)
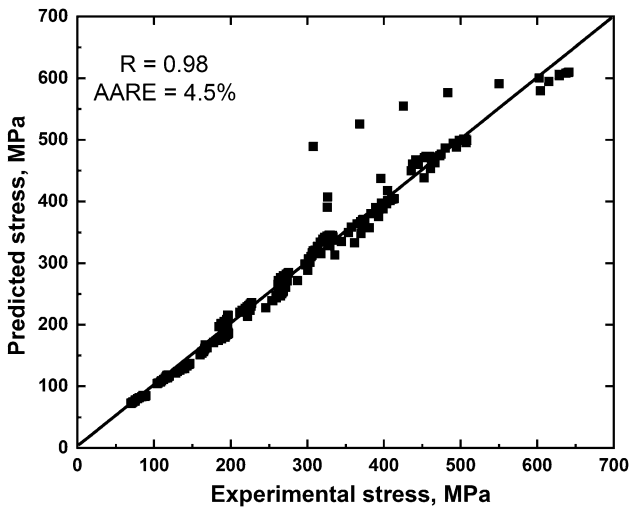

Fig. 13 Comparison between experimental flow stress and predicted flow stress calculated from apparent-based constitutive equation

Fig. 14 Comparison of predicted stress with experimental stress

3.5.1 Validation of a Constitutive Equation. To evaluate the prediction capability of a constitutive equation, two stress–strain curves randomly chosen corresponding to different temperatures 1323 and 1373 K and strain rates 10^{-2} and
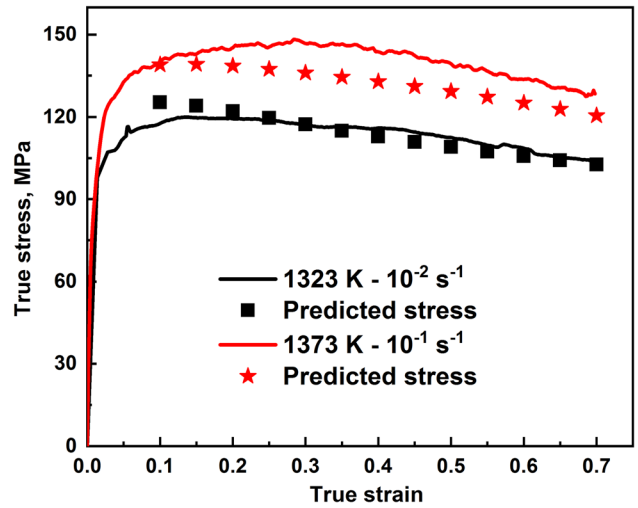
10^{-1} s^{-1} were eliminated during the calculation of material constants. Then the material constants obtained from the remaining stress–strain curves were employed to predict the

flow behavior of the aforementioned stress–strain curves as shown in Fig. 14. The predicted values are reasonably close to the experimental values. This indicates that the derived constitutive equation is reasonably good enough to predict the flow curve behavior within the studied temperature and strain rate regime.

3.6 Flow Stress Modeling Using ANN

Typically ANN architecture consists of one input layer, one output layer and at least one intermediary hidden layer and these layers are connected by neurons. The input and output layers in an ANN model represent the independent and dependent variables, respectively. The neurons in the hidden layer are used solely for computational purposes. During training, the main aim is minimization of the target error, i.e., (ANN output—known target) by adjusting the weights and biases for the corresponding input data. The biases and weights are adjusted using back-propagation (BP) which is the most widely used learning algorithm for multilayer perception (Ref 65, 66). In the present work, to model the flow stress, a three layer network is employed and the schematic of the network is shown in Fig. 15. The inputs chosen for the model are temperature, strain rate and strain, respectively. The output of the model is flow stress. Levenberg–Marquardt (L–M) algorithm is the most time-efficient in terms of training the model and the same has been employed in this study.

It is suggested that use of normalized data (both input and output) in the model allows the model to be more efficient. Therefore, before training of the network, input and output parameters are normalized to a range from 0.1 to 0.9. The most widely used equation for the normalization of the data is given below (Ref 67).

$$X' = 0.1 + 0.8x\left(\frac{X - X_{\min}}{X_{\max} - X_{\min}}\right) \quad \text{(Eq 28)}$$

where X' is the normalized data corresponding to X, X is the original data and $X_{\max}$ and $X_{\min}$ are the maximum and minimum values of X.

Eq 28 is used to normalize the temperature and flow stress data. The strain values are already within the 0.1-0.9, so, it need not be normalized further. It is not appropriate to use Eq 28 for normalizing the strain rate data directly or (as it is), because its value changes by several orders of magnitude and not uniformly distributed after normalization (Ref 68). Moreover, the normalized strain rate values obtained at lower strain rate is too small to be learned effectively by the ANN. Instead of strain rate, log (strain rate) is considered for the analysis, the equation employed for the normalization of strain rate is,

$$\dot{\varepsilon}' = 0.1 + 0.8x\left(\frac{\log\dot{\varepsilon} - \log\dot{\varepsilon}_{\min}}{\log\dot{\varepsilon}_{\max} - \log\dot{\varepsilon}_{\min}}\right) \quad \text{(Eq 29)}$$

The reliability of an ANN model largely depends on the number of input–output data sets used to train the model. The total number of data points collected from the experimental flow curves is 960. In which 80% of the data was used for
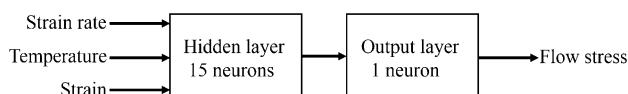
network training. This was accomplished by skipping the data points at regular intervals. The skipped data were used to test the prediction capability of the network. The parameters of the network used in the current work are listed in Table 3. During training, the model adjusts its weights through multiple passes of the provided input–output data. One complete pass of all input and output data is defined as an epoch. More the number of epochs, more accurate would be the results. The number of hidden neurons gives a measure of the complexity of the model. Too less a number would give inaccurate results. Thus for any ANN model to be efficient and accurate, the number of hidden neurons has to be optimized. The mean square error (MSE) was taken as a measure of the performance of the model. A target MSE of the order of 10^{-6} was set. MSE was calculated for varying number of hidden neurons. The iterations were stopped until the set target accuracy was achieved. Accordingly, in the present work the optimum number of hidden neurons was found to be 15, with an MSE of 2.64 e−06 after 570 epochs.

$$\text{MSE} = \frac{1}{n}\sum_{i=1}^{n}(e_i - p_i)^2 \quad \text{(Eq 30)}$$

where n is the total number of data sets, e_i is the experimentally measured value and p_i is the predicted value from ANN model.

The predicted flow stress obtained from ANN model showed very good agreement with the experimental results as shown in Fig. 16. The studied ANN model is able to predict the material flow behavior from 0.1 to 0.7 strain well, which including both stain hardening and flow softening. The calculated correlation coefficient of ANN model is almost close to 1 (0.999) which is higher than that of the apparent-based approach (0.98). In the flow stress values predicted by ANN model, most of the data points lie on the 45° line, which indicates that ANN model is more superior than the apparent-based approach. The AARE calculated from ANN model is 0.79% which is much smaller than that of the apparent-based approach (4.5%).

From the above results, it is evident that both models are good in predicting the flow stress. The advantage of apparent-based approach is that it provides a simple mathematical relation which can be incorporated in finite element method for the simulation of the flow behavior of material in the studied temperature and strain rate domain, whereas from ANN model, no mathematical or empirical relation can be drawn. Nevertheless, the generated ANN model can be used to predict the flow behavior.

3.7 Finite Element Simulation

Finite element simulations were used to validate the constitutive equation generated by data obtained from the experiments conducted in Gleeble as a generalized material

Table 3 The parameters of the ANN network used in the current work

Network type	Feed-forward backprop
Train function	TRAINLM
Adaption learning function	LEARNGDM
Performance function	MSE
Number of neurons	15
Transfer function	Sigmoid

Fig. 15 Schematic of ANN model

model. Finite element simulation package Simufact 14.0.1 was used for the simulation. A finite element model that replicates the Gleeble setup was used.

As the sample and process are axisymmetric, the problem was simplified into a 2-D axisymmetric one. Sample geometry was meshed with linear axisymmetric quadrilateral elements. An element edge length of 0.1 mm was used as shown in Fig. 17. Adaptive mesh refinement was also used to capture fine variations of the field variables. The adaptive mesh refinement algorithm automatically reduces mesh size where finer details are to be captured and uses coarser mesh wherever possible. This avoids errors due to mesh distortion without considerably increasing the computation time. A strain-based re-meshing algorithm was incorporated to avoid errors caused by excessive element distortion.

Analogous to the Gleeble fixtures, the bottom plate was assumed to be fixed and the top plate moving such that a constant average plastic strain rate is maintained. Accordingly, top plate velocity was calculated based on the equations shown below.

$$\dot{\varepsilon} = \frac{v}{h} \qquad (Eq\ 31)$$

$$v = \dot{\varepsilon} \times h \qquad (Eq\ 32)$$

where $\dot{\varepsilon}$ is the average true strain rate, v is the velocity of top plate, h is the instantaneous height of the sample.

Temperature distribution was assumed to be uniform before deformation. Gleeble uses feedback-controlled resistance heating technique to compensate for the heat losses to the atmosphere. The measurements from the thermocouple during the experiment were found to be in reasonable agreement with the predicted temperatures at the same point in the simulation.

The material was assumed to be homogenous to start with and follow von-Mises yield criterion and an associated flow rule with isotropic strain and strain rate hardening. The empirical sine hyperbolic relation (Eq 15) predicts the flow stress as a function of strain rate and temperature.

In order to incorporate the effect of strain in the stress predictor, the above said plots were fitted with polynomial Eq 24-27, as shown in Table 2. These data were incorporated into Eq 15 and were used as the material model for simulation. The same was incorporated into the simulation using a user-defined material sub-routine code written in FORTRAN77. During the simulation, the sub-routine function was called at each time step with the strain, strain rate and temperature as the input arguments.

Shear friction condition was assumed. A friction factor of 0.15 was arrived up on by correlating the barreling width in simulation with experiments. The assumption of constant shear friction condition throughout the process is sufficient for accurate prediction of force versus stroke curve and the barreling of the sample. Depending on the process, friction conditions and material, one may choose a suitably different friction model as well for accurate prediction of material flow field (Ref 69). The thermal coefficient of expansion, heat conductivity and specific heat capacity of the material was incorporated from existing data library (Ref 70, 71). The variation of these properties with respect to temperature was also taken into account. Also, a fraction of the deformation work gets converted to heat. This generally varies with strain rate.

Fraction of deformation work dissipated as heat $= 0.95 \times \eta$

$$(Eq\ 33)$$

where the heat generation efficiency factor (η) was calculated by the set of equations given below:

$$\eta = \begin{pmatrix} 0 & \text{when} & \dot{\varepsilon} < 10^{-3} \\ 0.316 \log(\dot{\varepsilon}) + 0.95 & \text{when} & 10^{-3} < \dot{\varepsilon} < 1 \\ 0.95 & \text{when} & \dot{\varepsilon} > 1 \end{pmatrix} \quad (Eq\ 34)$$

3.7.1 Simulation Results. In the experiment, the generated experimental stress–strain curves are average values. For a fair comparison, the average values of true stress versus true strain were calculated from the finite element simulation results. The data of force applied by the plate on the specimen and the plate displacement were made use of for the calculations. The true stress–true strain curves corresponding to hot compression
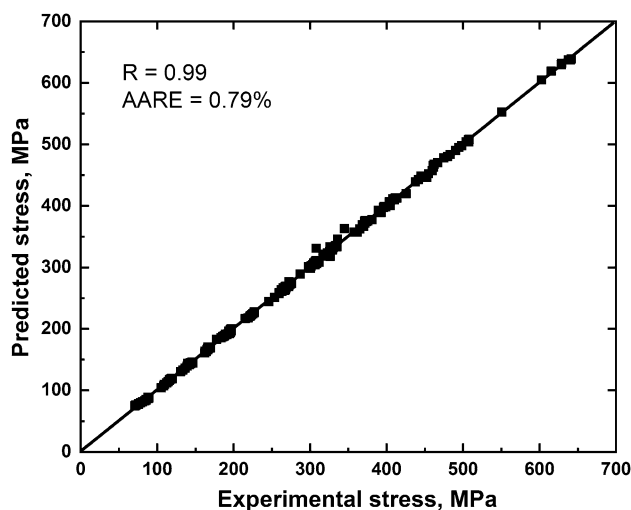

Fig. 16 Comparison between experimental flow stress and predicted flow stress calculated from artificial neural network model
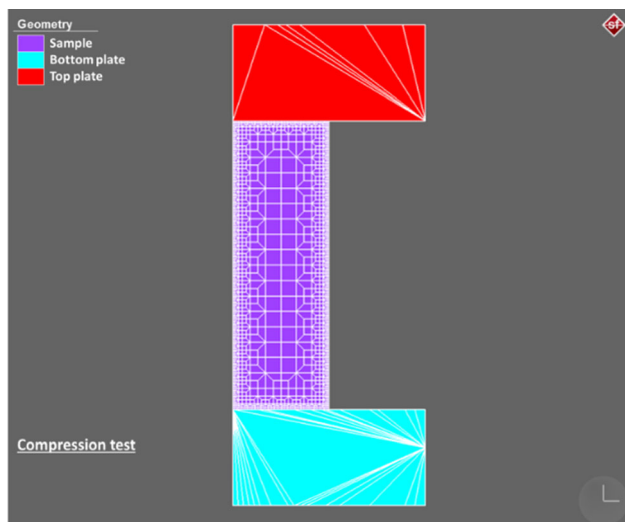

Fig. 17 Initial mesh generated for finite element simulation

at 0.1 s^{-1} strain rate, at a temperature of 1223 K obtained from experiment and simulation are shown in Fig. 18. The strain distribution predicted by the FE simulation of the same experiment after deformation is shown in Fig. 19. Strain distribution is not uniform as can be seen from the figure, with
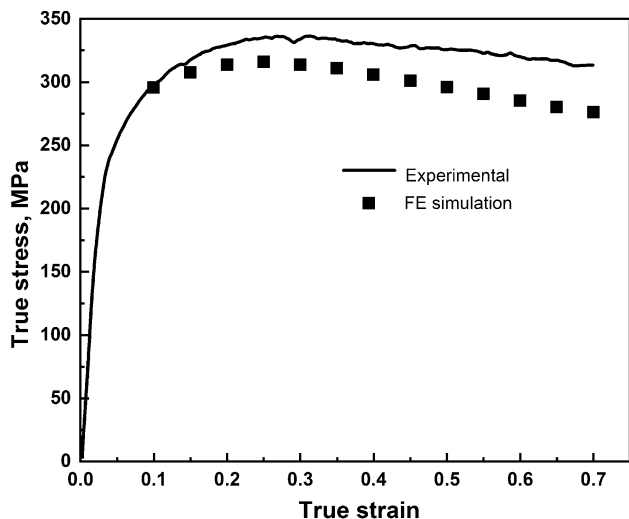
3 regions marked. Figure 20 shows the optical micrographs acquired from the corresponding regions. Region 1 labeled in the figure shows high strains, indicating high amount of deformation, reflected in the corresponding optical micrograph as can be seen in Fig. 20(a). Region 2 is the dead zone with negligible deformation, resulting in a nearly undeformed grain morphology as can be seen in Fig. 20(b). Region 3 lies between region 1 and the free surface of the sample and seems to have undergone lower strains compared to region 1. Figure 20(c) shows the corresponding grain morphology. Micro-Vickers hardness indentations with 1 kg load for a dwell time of 10 s were made at different locations on the sample before and after deformation. Before deformation, the sample showed a hardness value of 195 HV$_1$. Region 1 showed a hardness value of 270 HV$_1$, region 2, a hardness value of 215 HV$_1$ and region 3, a hardness value of 245 HV$_1$, which are consistent with the strain distribution map generated by FE simulation.

Figure 21 shows the temperature distribution of a sample compressed at 1373 K and 10 s^{-1} at a stroke position of 7.5 mm as predicted by the simulation. In accordance with strain distribution, the temperature is also the highest at the core and the lowest at the center of the contact surface. The adiabatic heat rise from the simulation (1406 K at periphery of the sample) is slightly higher than the experimental value [1400 K (see Fig. 3b)]. The slight difference could be due to the assumptions made in the simulation and material constants considered from the literature.
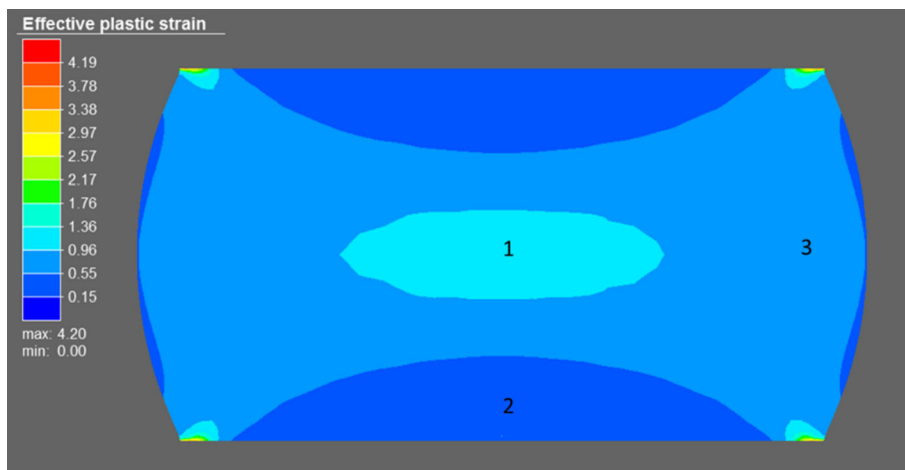

Fig. 18 Comparison of experimental curve at 1223 K, 10^{-1} s^{-1} with simulation data

Fig. 19 Strain distribution data in compression at 1223 K and 10^{-1} s^{-1}

(a) Region1: Centre   **(b)** Region 2: Dead zone   **(c)** Region 3: Near free surface
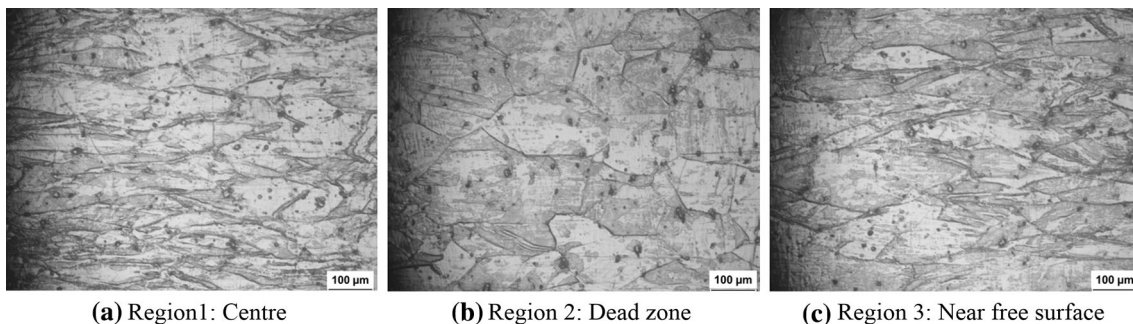
Fig. 20 Optical micrographs of a sample compressed at 1223 K and 10^{-1} s^{-1}
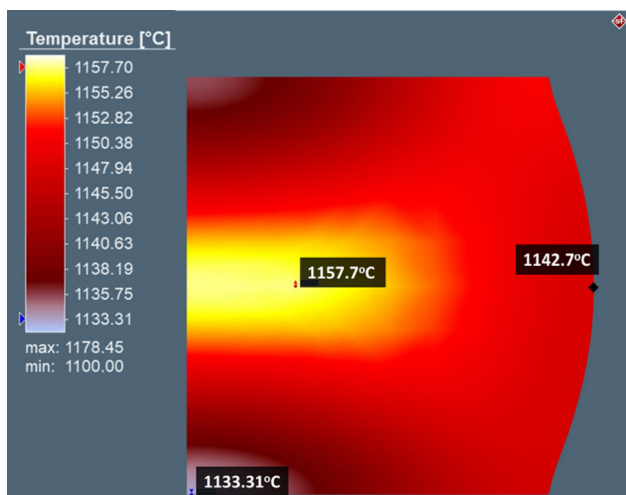
Fig. 21 Temperature distribution predicted by simulation at 7.5 mm stroke position

The sine hyperbolic equation is generally used for predicting the peak stress for any given temperature and strain rate. The use of the same as a material model, incorporating the effect of strain as well has been demonstrated. The true stress versus true strain curves predicted by the finite element simulations were found to match well with the actual experimental data. R and AARE values of the simulated data calculated with respect to the experimental values were 0.94 and 10.73%, respectively. These values are comparable to that of apparent-based approach. The above results confirm that the sine hyperbolic stress predictor can be used as a generalized material model in finite element simulation of Alloy 718 with reasonable accuracy.

4. Conclusions

1. Arrhenius type constitutive equations were derived to predict the peak flow stress by apparent and physically based approach:

$$\sigma_p = \frac{1}{0.00376}\sinh^{-1}\left(\frac{\dot{\varepsilon}\exp\left(\frac{477389}{RT}\right)}{3.07\times10^{18}}\right)^{1/4.4}$$

$$\sigma_p = \frac{E_{(T)}}{549}\sinh^{-1}\left(\frac{\dot{\varepsilon}\exp\left(\frac{285000}{RT}\right)}{2.2\times10^{10}}\right)^{1/5}$$

2. Peak flow stress predicted from apparent-based approach showed better statistical performance ($R = 0.99$, AARE = 6%) compared to that of physically based approach ($R = 0.96$, AARE = 18%).
3. Dislocation climb was found to be the rate controlling mechanism operated in the studied range of temperature (1223-1373 K) and strain rate (10^{-2} s^{-1}-10 s^{-1}).
4. Based on statistical analysis, it is found that ANN method is better than the derived constitutive equation to predict the flow stress.
5. Strain compensated constitutive equation was used as a material model for FE simulation. Flow stress values pre-

dicted by the simulation were comparable to the experimental results.
6. The equivalent plastic strain distribution of the deformed sample predicted by FE simulation showed a trend similar to the Vickers hardness measurements and the microstructure observed.

References

1. W.D. Cao and R.L. Kennedy, Superalloys 718, 625, 706 and Various Derivatives, Ed, *EA Loria, TMS* (2001), p 455–464
2. A. Thomas, M. El-Wahabi, J.M. Cabrera, and J.M. Prado, High Temperature Deformation of Inconel 718, *J. Mater. Process. Technol.*, 2006, **177**(1–3), p 469–472
3. L.C.M. Valle, L.S. Araújo, S.B. Gabriel, J. Dille, and L.H. De Almeida, The Effect of δ Phase on the Mechanical Properties of an Inconel 718 Superalloy, *J. Mater. Eng. Perform.*, 2013, **22**(5), p 1512–1518
4. M.J. Sohrabi, H. Mirzadeh, and M. Rafiei, Solidification Behavior and Laves Phase Dissolution during Homogenization Heat Treatment of Inconel 718 Superalloy, *Vacuum*, 2018, **154**, p 235–243
5. M.J. Sohrabi and H. Mirzadeh, Unexpected Formation of Delta (δ) Phase in as-Cast Niobium-Bearing Superalloy at Solution Annealing Temperatures, *Mater. Lett.*, 2020, **261**, p 127008
6. S. Azadian, L.-Y. Wei, and R. Warren, Delta Phase Precipitation in Inconel 718, *Mater. Charact.*, 2004, **53**(1), p 7–16
7. D.D. Krueger, The Development of Direct Age 718 for Gas Turbine Engine Disk Applications, *Superalloy 718 Metall. Appl.* 279–296 (1989)
8. H.Y. Zhang, S.H. Zhang, M. Cheng, and Z.X. Li, Deformation Characteristics of δ Phase in the Delta-Processed Inconel 718 Alloy, *Mater. Charact.*, 2010, **61**(1), p 49–53. https://doi.org/10.1016/j.matc har.2009.10.003
9. H. Zhang, K. Zhang, Z. Lu, C. Zhao, and X. Yang, Hot Deformation Behavior and Processing Map of a γ′-Hardened Nickel-Based Superalloy, *Mater. Sci. Eng. A*, 2014, **604**, p 1–8. https://doi.org/10.1016/j. msea.2014.03.015
10. M. Azarbarmas, M. Aghaie-Khafri, J.M. Cabrera, and J. Calvo, Microstructural Evolution and Constitutive Equations of Inconel 718 Alloy under Quasi-Static and Quasi-Dynamic Conditions, *Mater. Des.*, 2016, **94**, p 28–38. https://doi.org/10.1016/j.matdes.2015.12.157
11. Y.B. Tan, Y.H. Ma, and F. Zhao, Hot Deformation Behavior and Constitutive Modeling of Fine Grained Inconel 718 Superalloy, *J. Alloys Compd.*, 2018, **741**, p 85–96
12. S.A. Sajjadi, A. Chaichi, H.R. Ezatpour, A. Maghsoudlou, and M.A. Kalaie, Hot Deformation Processing Map and Microstructural Evaluation of the Ni-Based Superalloy IN-738LC, *J. Mater. Eng. Perform.*, 2016, **25**(4), p 1269–1275
13. A. Amiri, M.H. Sadeghi, and G.R. Ebrahimi, Characterization of Hot Deformation Behavior of AMS 5708 Nickel-Based Superalloy Using Processing Map, *J. Mater. Eng. Perform.*, 2013, **22**(12), p 3940–3945
14. Z. Shi, X. Yan, C. Duan, C. Tang, and E. Pu, Characterization of the Hot Deformation Behavior of a Newly Developed Nickel-Based Superalloy, *J. Mater. Eng. Perform.*, 2018, **27**(4), p 1763–1776
15. S.S.S. Kumar, T. Raghu, P.P. Bhattacharjee, G.A. Rao, and U. Borah, Strain Rate Dependent Microstructural Evolution during Hot Deformation of a Hot Isostatically Processed Nickel Base Superalloy, *J. Alloys Compd.*, 2016, **681**, p 28–42. https://doi.org/10.1016/j.jallcom. 2016.04.185
16. Z. Wan, L. Hu, Y. Sun, T. Wang, and Z. Li, Hot Deformation Behavior and Processing Workability of a Ni-Based Alloy, *J. Alloys Compd.*, 2018, **769**, p 367–375. https://doi.org/10.1016/j.jallcom.2018.08.010
17. S.B. Davenport, N.J. Silk, C.N. Sparks, and C.M. Sellars, Development of Constitutive Equations for Modelling of Hot Rolling, *Mater. Sci. Technol.*, 2000, **16**(5), p 539–546. https://doi.org/10.1179/026708300 101508045
18. J. Luo, M. Li, X. Li, and Y. Shi, Constitutive Model for High Temperature Deformation of Titanium Alloys Using Internal State Variables, *Mech. Mater.*, 2010, **42**(2), p 157–165. https://doi.org/10. 1016/j.mechmat.2009.10.004

19. Y.C. Lin, Q.F. Li, Y.C. Xia, and L.T. Li, A Phenomenological Constitutive Model for High Temperature Flow Stress Prediction of Al-Cu-Mg Alloy, *Mater. Sci. Eng. A*, 2012, **534**, p 654–662. https://doi.org/10.1016/j.msea.2011.12.023

20. H.Y. Li, D.D. Wei, J.D. Hu, Y.H. Li, and S.L. Chen, Constitutive Modeling for Hot Deformation Behavior of T24 Ferritic Steel, *Comput. Mater. Sci.*, 2012, **53**(1), p 425–430. https://doi.org/10.1016/j.commatsci.2011.08.031

21. S.A.S. Vanini, M. Abolghasemzadeh, and A. Assadi, Generalized Constitutive-Based Theoretical and Empirical Models for Hot Working Behavior of Functionally Graded Steels, *Metall. Mater. Trans. A Phys. Metall. Mater. Sci.*, 2013, **44**(7), p 3376–3384

22. L. Zhou, C. Cui, Q.Z. Wang, C. Li, B.L. Xiao, and Z.Y. Ma, Constitutive Equation and Model Validation for a 31 Vol.% B4Cp/6061Al Composite during Hot Compression, *J. Mater. Sci. Technol.*, 2018, **34**(10), p 1730–1738

23. R. Bobbili and V. Madhu, Constitutive Modeling of Hot Deformation Behavior of High-Strength Armor Steel, *J. Mater. Eng. Perform.*, 2016, **25**(5), p 1829–1838

24. Q. Zhao, L. Yu, Y. Liu, Y. Huang, Z. Ma, H. Li, and J. Wu, Microstructure and Tensile Properties of a 14Cr ODS Ferritic Steel, *Mater. Sci. Eng. A*, 2016, **2017**(680), p 347–350. https://doi.org/10.1016/j.msea.2016.10.118

25. R. Wang, M. Wang, Z. Li, and C. Lu, Physics-Based Constitutive Model for the Hot Deformation of 2Cr11Mo1VNbN Martensitic Stainless Steel, *J. Mater. Eng. Perform.*, 2018, **27**(9), p 4932–4940

26. L. Ou, Y. Nie, and Z. Zheng, Strain Compensation of the Constitutive Equation for High Temperature Flow Stress of a Al-Cu-Li Alloy, *J. Mater. Eng. Perform.*, 2014, **23**(1), p 25–30

27. M.R. Rokni, A. Zarei-Hanzaki, C.A. Widener, and P. Changizian, The Strain-Compensated Constitutive Equation for High Temperature Flow Behavior of an Al-Zn-Mg-Cu Alloy, *J. Mater. Eng. Perform.*, 2014, **23**(11), p 4002–4009

28. E.I. Poliak and J.J. Jonas, A One-Parameter Approach to Determining the Critical Conditions for the Initiation of Dynamic Recrystallization, *Acta Mater.*, 1996, **44**(1), p 127–136

29. H. Mirzadeh and A. Najafizadeh, Prediction of the Critical Conditions for Initiation of Dynamic Recrystallization, *Mater. Des.*, 2010, **31**(3), p 1174–1179. https://doi.org/10.1016/j.matdes.2009.09.038

30. A. Najafizadeh and J.J. Jonas, Predicting the Critical Stress for Initiation of Dynamic Recrystallization, *ISIJ Int.*, 2006, **46**(11), p 1679–1684. https://doi.org/10.2355/isijinternational.46.1679

31. S. Saadatkia, H. Mirzadeh, and J.M. Cabrera, Hot Deformation Behavior, Dynamic Recrystallization, and Physically-Based Constitutive Modeling of Plain Carbon Steels, *Mater. Sci. Eng. A*, 2015, **636**, p 196–202. https://doi.org/10.1016/j.msea.2015.03.104

32. Y. Wang, W.Z. Shao, L. Zhen, and B.Y. Zhang, Hot Deformation Behavior of Delta-Processed Superalloy 718, *Mater. Sci. Eng. A*, 2011, **528**(7–8), p 3218–3227. https://doi.org/10.1016/j.msea.2011.01.013

33. P. Páramo-Kañetas, U. Özturk, J. Calvo, J.M. Cabrera, and M. Guerrero-Mata, High-Temperature Deformation of Delta-Processed Inconel 718, *J. Mater. Process. Technol.*, 2017, **2018**(255), p 204–211. https://doi.org/10.1016/j.jmatprotec.2017.12.014

34. Y. Estrin and H. Mecking, A Unified Phenomenological Description of Work Hardening and Creep Based on One-Parameter Models, *Acta Metall.*, 1984, **32**(1), p 57–70

35. Y. Bergström, A Dislocation Model for the Stress–Strain Behaviour of Polycrystalline α-Fe with Special Emphasis on the Variation of the Densities of Mobile and Immobile Dislocations, *Mater. Sci. Eng.*, 1970, **5**(4), p 193–200

36. R. Gujrati, C. Gupta, J.S. Jha, S. Mishra, and A. Alankar, Understanding Activation Energy of Dynamic Recrystallization in Inconel 712, *Mater. Sci. Eng. A*, 2018, **744**, p 638–651. https://doi.org/10.1016/j.msea.2018.12.008

37. C. Gupta, J.S. Jha, B. Jayabalan, R. Gujrati, A. Alankar, and S. Mishra, Correlating Hot Deformation Parameters with Microstructure Evolution during Thermomechanical Processing of Inconel 718 Alloy, *Metall. Mater. Trans. A Phys. Metall. Mater. Sci.*, 2019, **50**(10), p 4714–4731. https://doi.org/10.1007/s11661-019-05380-0

38. S.S. Satheesh Kumar, T. Raghu, P.P. Bhattacharjee, G. Appa Rao, and U. Borah, Constitutive Modeling for Predicting Peak Stress Characteristics during Hot Deformation of Hot Isostatically Processed Nickel-Base Superalloy, *J. Mater. Sci.*, 2015, **50**(19), p 6444–6456

39. N. Haghdadi, A. Zarei-Hanzaki, A.R. Khalesian, and H.R. Abedi, Artificial Neural Network Modeling to Predict the Hot Deformation Behavior of an A356 Aluminum Alloy, *Mater. Des.*, 2013, **49**, p 386–391. https://doi.org/10.1016/j.matdes.2012.12.082

40. J. Zhao, H. Ding, W. Zhao, M. Huang, D. Wei, and Z. Jiang, Modelling of the Hot Deformation Behaviour of a Titanium Alloy Using Constitutive Equations and Artificial Neural Network, *Comput. Mater. Sci.*, 2014, **92**, p 47–56. https://doi.org/10.1016/j.commatsci.2014.05.040

41. S. Mandal, P.V. Sivaprasad, S. Venugopal, and K.P.N. Murthy, Artificial Neural Network Modeling to Evaluate and Predict the Deformation Behavior of Stainless Steel Type AISI, 304L during Hot Torsion, *Appl. Soft Comput. J.*, 2009, **9**(1), p 237–244

42. H. Mirzadeh, J.M. Cabrera, and A. Najafizadeh, Constitutive Relationships for Hot Deformation of Austenite, *Acta Mater.*, 2011, **59**(16), p 6441–6448. https://doi.org/10.1016/j.actamat.2011.07.008

43. N.K. Park, I.S. Kim, Y.S. Na, and J.T. Yeom, Hot Forging of a Nickel-Base Superalloy, *J. Mater. Process. Technol.*, 2001, **111**(1–3), p 98–102

44. Y. Wang, W.Z. Shao, L. Zhen, and X.M. Zhang, Microstructure Evolution during Dynamic Recrystallization of Hot Deformed Superalloy 718, *Mater. Sci. Eng. A*, 2008, **486**(1–2), p 321–332

45. N. Nayan, S.V.S.N. Murty, S. Chhangani, A. Prakash, M. Prasad, and I. Samajdar, Effect of Temperature and Strain Rate on Hot Deformation Behavior and Microstructure of Al-Cu-Li Alloy, *J. Alloys Compd.*, 2017, **723**, p 548–558

46. C. Zener and J.H. Hollomon, Effect of Strain Rate Upon Plastic Flow of Steel, *J. Appl. Phys.*, 1944, **15**(1), p 22–32

47. H.J. Mcqueen and N.D. Ryan, Constitutive Analysis in Hot Working, *Mater. Sci. Eng. A*, 2002, **322**, p 43–63

48. C.M. Sellars and W.J.M. Tegart, Relationship Between Strength and Structure in Deformation at Elevated Temperatures, *Mem. Sci. Rev. Met.*, **63**(9) (1966)

49. C.M. Sellars and W.J. McTegart, On the Mechanism of Hot Deformation, *Acta Metall.*, 1966, **14**(9), p 1136–1138

50. F. Garofalo, An Empirical Relation Defining the Stress Dependence of Minimum Creep Rate in Metals, *Trans. AIME*, 1963, **227**, p 351–356

51. H. Yuan and W.C. Liu, Effect of the δ Phase on the Hot Deformation Behavior of Inconel 718, *Mater. Sci. Eng. A*, 2005, **408**(1–2), p 281–289

52. W.J. Weis, *Superalloy 718-Metallurgy and Applications*, vol. 257 (Warrendale, 1989), p 135

53. C.I. Garcia, D.E. Camus, E.A. Loria, and A.J. DeArdo, *Superalloys 718, 625, 706 and Various Derivatives* (Warrendale, 1991), p 925

54. H.J. Frost and M.F. Ashby, *Deformation Mechanism Maps: The Plasticity and Creep of Metals and Ceramics*, Pergamon Press, London, 1982

55. H. Mirzadeh, M. Roostaei, M.H. Parsa, and R. Mahmudi, Rate Controlling Mechanisms during Hot Deformation of Mg-3Gd-1Zn Magnesium Alloy: Dislocation Glide and Climb, Dynamic Recrystallization, and Mechanical Twinning, *Mater. Des.*, 2015, **68**, p 228–231

56. Z. Bi, M. Zhang, J. Dong, K. Luo, and J. Wang, A New Prediction Model of Steady State Stress Based on the Influence of the Chemical Composition for Nickel-Base Superalloys, *Mater. Sci. Eng. A*, 2010, **527**(16–17), p 4373–4382

57. J.M. Cabrera, Modelling and Simulations in Hot Deformation of Steels, *Adv. Technol. Mater. Mater. Process. J.*, 2002, **4**(1), p 45–57

58. J.M. Cabrera, A. AlOmar, J.J. Jonas, and J.M. Prado, Modeling the Flow Behavior of a Medium Carbon Microalloyed Steel under Hot Working Conditions, *Metall. Mater. Trans. A*, 1997, **28**(11), p 2233–2243

59. H. Mirzadeh, Constitutive Description of 7075 Aluminum Alloy During Hot Deformation by Apparent and Physically-Based Approaches, *J. Mater. Eng. Perform.*, 2015, **24**(3), p 1095–1099

60. G.E. Dieter and D.J. Bacon, *Mechanical Metallurgy*, Mc'Graw-Hill, New York, 1986

61. M.P. Phaniraj and A.K. Lahiri, The Applicability of Neural Network Model to Predict Flow Stress for Carbon Steels, *J. Mater. Process. Technol.*, 2003, **141**(2), p 219–227

62. S. Srinivasulu and A. Jain, A Comparative Analysis of Training Methods for Artificial Neural Network Rainfall-Runoff Models, *Appl. Soft Comput. J.*, 2006, **6**(3), p 295–306

63. K.P. Rao and E.B. Hawbolt, Development of Constitutive Relation-

ships Using Compression Testing of a Medium Carbon Steel, *J. Eng. Mater. Technol. Trans. ASME*, 1992, **114**(1), p 116–123

64. H. Mirzadeh, A Simplified Approach for Developing Constitutive Equations for Modeling and Prediction of Hot Deformation Flow Stress, *Metall. Mater. Trans. A*, 2015, **46**(9), p 4027–4037. https://doi.org/10.1007/s11661-015-3006-1

65. K. Genel, S.C. Kurnaz, and M. Durman, Modeling of Tribological Properties of Alumina Fiber Reinforced Zinc-Aluminum Composites Using Artificial Neural Network, *Mater. Sci. Eng. A*, 2003, **363**(1–2), p 203–210

66. A. Mirzaei, A. Zarei-Hanzaki, M.H. Pishbin, A. Imandoust, and S. Khoddam, Evaluating the Hot Deformation Behavior of a Super-Austenitic Steel through Microstructural and Neural Network Analysis, *J. Mater. Eng. Perform.*, 2015, **24**(6), p 2412–2421

67. J. Liu, H. Chang, T.Y.H. Xu, and X. Ruan, Prediction of the Flow Stress of High-Speed Steel during Hot Deformation Using a BP Artificial Neural Network, *J. Mater. Process. Technol.*, 2000, **103**, p 200–205

68. H. Mirzadeh, J.M. Cabrera, and A. Najafizadeh, Modeling and Prediction of Hot Deformation Flow Curves, *Metall. Mater. Trans. A Phys. Metall. Mater. Sci.*, 2012, **43**(1), p 108–123

69. D. Kundalkar, R. Singh, and A. Tewari, Effect of Friction Models and Parameters on the Lagrangian Flow Fields in High-Temperature Compression Testing, *J. Mater. Eng. Perform.*, 2017, **26**(10), p 4867–4875

70. High Tmperature Inconel 718, 2014. http://www.hightempmetals.com/techdata/hitempInconel718data.php. Accessed 14 March 2014

71. Inconel Alloy 718, 2014. http://www.specialmetals.com/documents/Inconelalloy718.pdf. Accessed 14 March 2014